Thermal Characterization of Microheated Microchannels With Spatially Resolved Two-Color Fluorescence Thermometry

Tae Jin Kim, *Member, IEEE*, Myeongsub Kim, Sungyun Hann, Juan Trejo, and Carlos H. Hidrovo

***Abstract*— Two-color fluorescence thermometry is a well known, noninvasive, and accurate technique used to measure temperature in liquids. In this paper, we present an improved methodology that enhances the spatial accuracy of the technique by minimizing image-pair distortion errors and its subsequent use in the characterization of heated microchannels. In order to spatially calibrate the image-pair and to quantify the distortion of one image with respect to the other, particle image velocimetry was performed with sandpaper. Results show that the objective lens and the primary dichroic mirror does not significantly affect the beam path and that the main source of distortion is likely to occur between the secondary dichroic mirror and the reflective mirrors within the emission splitting system. This spatial calibration and correlation methodology was used to map the temperature distribution in microheated microchannels. The experimentally calculated advective efficiency results showed good agreement against their numerically computed counterparts. These results suggest that the power supplied to the microheaters should be varied accordingly to maintain fixed heat flux conditions through the microchannel walls as a function of flow rate. [2014-0041]**

***Index Terms*— Optical distortion, fluorescence, microfluidics, thermal analysis, heating.**

I. Introduction

LAB-ON-A-CHIP devices such as micro-heat exchangers [1]–[4], micro-mixers [5], [6], polymerase chain reaction (PCR) microchips [7], [8] and microfluidic incubators [9]–[11] require careful control of the transport properties due to the complexity of microfluidic networks and integrated sensors/controllers. While the fluid transport can be characterized through non-invasive methods, quantifying the thermal transport has been proven to be more difficult. The traditional method to quantify temperature in microchannels is to estimate the mean wall-fluid temperature difference by comparing multiple thermocouple readings at the vicinity of the microchannel walls and the averaged inlet and outlet fluid temperatures [12]–[14]. In order to reduce the conduction effects between the wall and the thermocouples, methods such as fabricating resistance thermometers near the microchannel walls [15] were also implemented. However, embedding or fabricating such thermal sensors is limited by the spatial resolution as well as the number of sensing locations.

One method to accurately measure the fluid temperature in a minimally intrusive manner is through the use of temperature sensitive dyes [16], [17], where application to microchannels has been recently introduced [18]–[20]. However, since such method involves the use of two emission signals from a single source, spatial calibration is required to ensure that each pixel is consistently imaging the identical coordinate. In larger scale experiments for stereoscopic particle image velocimetry (PIV) applications, grid pattern plates were used to calibrate the image coordinates [21] and the errors associated with each camera were measured to be 1.1 pixels and 1.2 pixels [22]. Another method to spatially correct ratiometric images was introduced by Hidrovo and Hart [23], where spatial calibration was performed based on the PIV technique on sandpaper images. While spatial calibration has been performed to improve accuracy of ratiometric images, it has been brought to attention that spatial calibration and identification of the discrepancy source for microfluidic fluorescence thermometry applications has not been performed to date.

In the current experiment, an emission splitting system (DV2, Photometrics) is used to perform the two-color thermometry in heated microchannels. While the conventional method to perform microscope thermometry is through manual switching between two dichroic mirror cubes in the microscope, this method may induce error due to the fluctuating laser power intensity with time [24]. The emission splitting system has the advantage of resolving temporal discrepancy for each set of frame, but due to the limiting dimensions when imaging microchannels, an offset of a few pixels may result in a large error. Thus, the spatial calibration must be performed to resolve possible distortion of the image. The sandpaper PIV method has been implemented to quantify the distortion effects of the two emission images and to compare the effects on image distortion using different objective lens and dichroic mirrors.

With the corrected spatial information, two-color fluorescence thermometry was performed on a microchannel

Manuscript received February 10, 2014; revised April 1, 2014; accepted April 18, 2014. Date of publication May 20, 2014; date of current version January 30, 2015. This work was supported by the University of Texas at Austin, Austin, TX, USA; in part by the Science and Technology Acquisition and Retention Program, University of Texas System; and in part by Northeastern University, Boston, MA, USA. Subject Editor S. Shoji.

T. J. Kim and C. H. Hidrovo are with Northeastern University, Boston, MA 02115 USA (e-mail: ta.kim@neu.edu; hidrovo@neu.edu).

M. Kim and S. Hann are with the University of Texas at Austin, Austin, TX 78712 USA (e-mail: mskim@utexas.edu; sungyun.hann@utexas.edu).

J. Trejo was with the University of Texas at Austin, Austin, TX 78712 USA. He is now with Cummins Corporation, Columbus, IN 47202 USA (e-mail: jtrejo13@utexas.edu).

Color versions of one or more of the figures in this paper are available online at http://ieeexplore.ieee.org.

Digital Object Identifier 10.1109/JMEMS.2014.2320998

1057-7157 © 2014 IEEE. Personal use is permitted, but republication/redistribution requires IEEE permission.
See http://www.ieee.org/publications_standards/publications/rights/index.html for more information.

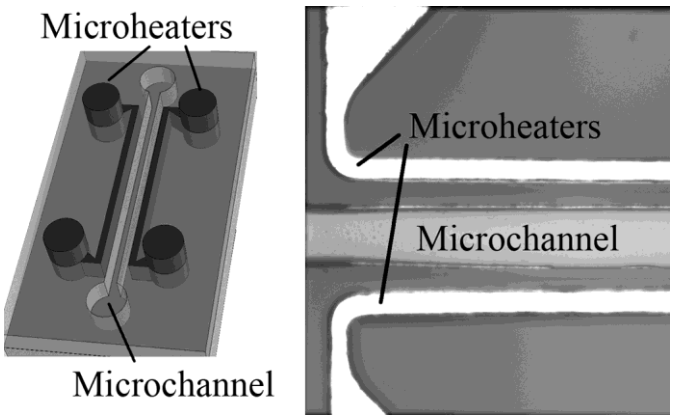

Fig. 1. Schematic diagram (left) and micrograph (right) of a microheater device embedded near the side walls of the microchannel.

with heating from the side walls. The microheaters were fabricated by flowing molten solder through satellite microchannels aligned next to the liquid phase microchannel [25], and heating was applied by flowing current through the solidified microheaters. By assessing the corresponding advective efficiency in the heated sections and comparing with numerical results, this study aims to provide an in-depth thermal analysis of microchannel flows with complex structures or wall conditions [26]–[28] with a high accuracy.

II. Materials and Methods

A. Fabrication of Microheater Embedded PDMS Microchannels

The microheater embedded PDMS microchannel design consists of three parallel microchannels, where the main microchannel is positioned between the two satellite microheater channels which provide side wall heating (Fig. 1). Su-8 molds with two different microchannel dimensions were fabricated with Su-8 2075 (Microchem) photoresists using photolithographic procedures. On the silicon wafer, a positive replica of the liquid microchannel with dimensions of 100μm $\times$ 50μm $\times$ 20mm (width $\times$ height $\times$ length) and 100μm $\times$ 100μm $\times$ 20mm were fabricated. Two pressure taps before and after the microchannels were designed to measure the pressure drop of the fluid. For the joule heater section, two satellite microchannels with cross-sectional area of 40μm $\times$ 50μm (width $\times$ height) 40μm $\times$ 100μm, corresponding to the two main microchannel heights, were located 40μm away from the main microchannel in order to fill it with the low melting temperature alloy.

Once the Su-8 mold was completed, a negative replica of the PDMS microchannel was fabricated using standard soft lithographic procedures and was bonded to a slide glass with oxygen plasma treatment (PDC-001, Harrick Plasma). The bonded microchannels were then stored overnight under standard atmospheric conditions.

For the microheater section, a low melting point alloy (Bismuth 58% and Tin 42%, Rotometals) with a melting temperature of 140 °C was used. This alloy was selected due to a number of advantages: 1) the alloy is lead-free and is thus low in toxicity, 2) as indicated by Siegal *et al.* [25], the use of low melting point metal alloys to fabricate microfeatures is a cost effective approach compared to fabricating film heaters through lithography with expensive materials, and 3) the melting temperature is higher than the water boiling temperature but is within the working temperature of the PDMS [29].

The solder was preheated on a hot plate at 160 °C along with the syringe needle that is used as the pressure source and was dispensed on top of the inlet tube. Positive pressure below 10 psi was applied by covering the entire inlet hole along with the solder using a 5-gage dispensing needle and the molten solder was flown into the satellite microchannels.

B. Fluid Flow and Fluorescence Thermometry

Water flow in the main microchannel was controlled via a pneumatically pressurized water reservoir (Fig. 2(a)). The pressure was controlled using a regulator (QPV1, Proportion-air) connected to a compressed air line. The input pressure was set until the target flow rate and the microheater power reached steady state (Table I), where the volumetric flow rate was measured using a liquid flowmeter (SLG-0430 and SLG-1000, Sensirion). Prior to loading the microchannel, air bubbles trapped in the PDMS-glass interface were removed by filling the microchannel with water and storing it in a vacuum chamber for approximately an hour under ~20 inches Hg. Although the dissolved air content in the working fluid is not likely to affect the heat transfer in the current temperature range [30], the fluorophore solution was degassed as well for at least 30 minutes prior to the experiment.

The fluid temperatures in the heated microchannel sections were measured using temperature sensitive fluorescence dyes [31]. In an optically thin medium, the fluorescent intensity is expressed as,

$$I_{em} = \Phi(T) I_0 (1 - e^{-\varepsilon(\lambda, pH)Ct}) \approx \Phi(T) I_0 \varepsilon C t \qquad (1)$$

where Φ is the quantum yield, I_0 is the excitation intensity, ε is the absorption (extinction) coefficient, C is the concentration of the fluorescent solution, and t is the solution thickness. At constant pH, C, t and with a single, uniform and stable light source, it is possible to measure solution temperatures from the fluorescent intensities since the quantum yield of the fluorophore is dependent on temperature. However, since the excitation intensity from the light source usually involves spatial and temporal variation, these variations in I_o should be decoupled from the emission intensity I_{em} for accurate temperature measurements.

C. Two-Color Fluorescence Thermometry

To decouple I_{em} from I_o and t, two-color fluorescence thermometry is performed by taking the ratio of two fluorescent dyes,

$$\frac{I_{em,1}}{I_{em,2}} \approx \frac{\Phi_1 C_1 \varepsilon_1(\lambda, pH)}{\Phi_2 C_2 \varepsilon_2(\lambda, pH)} \qquad (2)$$

where the intensity ratio becomes a function of temperature only as long as the pH, C_1 and C_2 are constant. The advantage

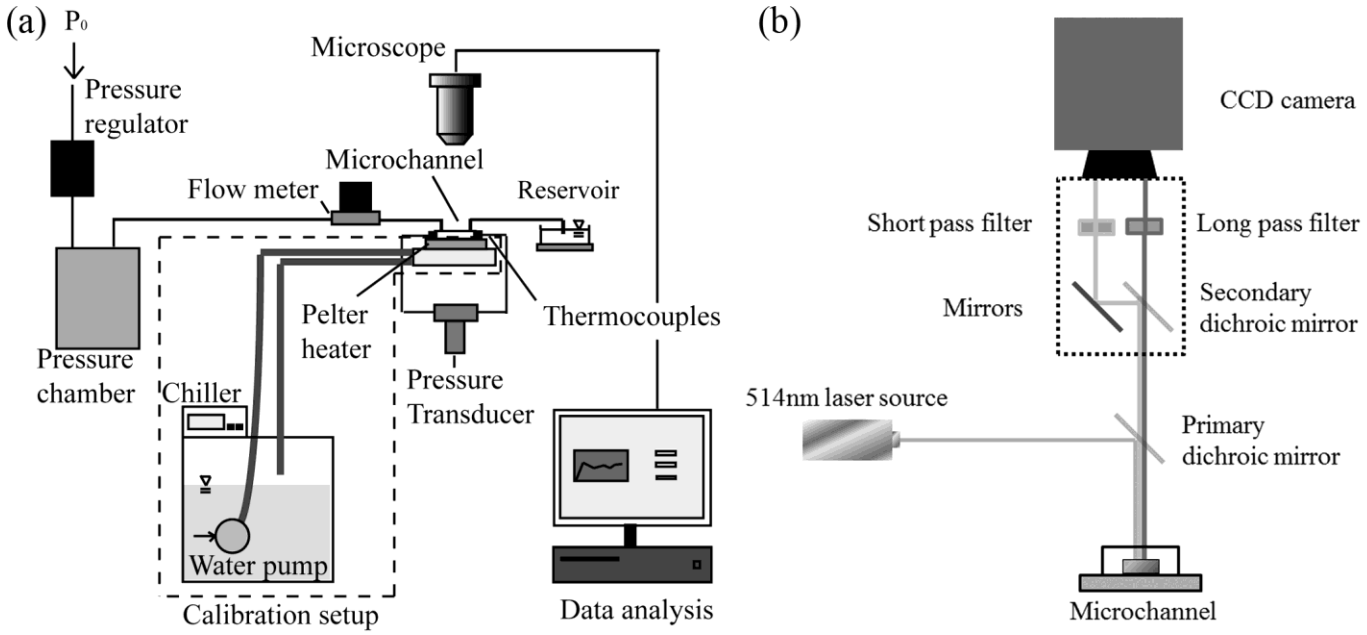

Fig. 2. Schematic diagram of the (a) differential pressure source setup, where the dashed line represents the setup used for fluorescence intensity versus temperature calibration, and the (b) fluorescence emission splitter setup. The dotted line represents the optics inside the emission splitting system.

TABLE I
GENERAL EXPERIMENTAL PARAMETERS

Parameters	Values
Input pressure	250 – 20,700 (Pa)
Flow rate	10 – 290 (μl/min)
Microheater power	0.11 – 0.72 (W)

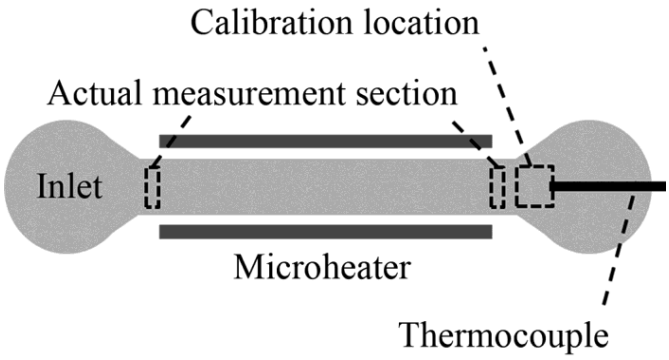

Fig. 3. Schematic diagram of the temperature measurement and calibration scheme. The temperature calibration is performed by collecting micrographs near the microchannel outlet and upstream of the hypodermic thermocouple tip.

of two-color fluorescence thermometry is that it is a minimally invasive method through the use of soluble fluorophores that are highly sensitive to temperature changes [16]. In this study, fluorescein (Fl) and Sulforhodamine B (SrB) were selected as the two fluorophores due to their poor adsorption to the PDMS surface, thus increasing the signal-to-noise ratio [19]. The optically thin condition was satisfied by setting the concentration of both fluorophores to 30μmol/L, and the solution pH was determined to be 8.5 so that the quantum yield of Fl is maximized (note that emission intensities of SrB is pH-independent). Since the fluorophore extinction coefficient is dependent on pH, the working solution was prepared with 0.1mol/L Phosphate Buffered Saline solution in order to mitigate pH changes in the solution.

An argon-ion laser at a wavelength of 514nm (Stellar-Pro Select 150, Modu-laser) was used to excite the fluorophores, and the Fl and SrB emissions were isolated by an emission splitting system (DV2, Photometrics). In the microscope, a dichroic mirror close to the sample reflects at or below the excitation wavelength ($\lambda = 514$nm) while it transmits fluorescent emissions with longer wavelengths. In the emission splitting system, a secondary dichroic mirror transmits the Fl emissions at wavelengths $\lambda < 561$nm and reflects the longer SrB emission wavelengths at $\lambda > 561$nm. The Fl and SrB emissions are cleaned by passing through a short bandpass filter which transmits wavelengths $\lambda = 522 - 552$nm (ET537/29m, Chroma) and a longpass filter that transmits the wavelengths $\lambda = 590 - 650$nm (HQ620/60m, Chroma), respectively (Fig. 2(b)). The corresponding emission data were collected with a scientific charge-coupled detector (CCD) device (Coolsnap HQ Diff, Photometrics).

In order to correlate the fluorescent intensity ratio to the actual temperature of the solution, in situ calibration was performed within the actual PDMS microchannel (dashed line in Fig. 2(a)). A thermoelectric Peltier heater was placed underneath the microchannel to provide constant temperature conditions where the temperature was consistently monitored with a T-type hypodermic thermocouple (HYP0, Omega) embedded near the microchannel outlet. A 10X objective lens (NA=0.3, Nikon Microscopes) was used to focus the region of interest where the thermocouple is located (Fig. 3).

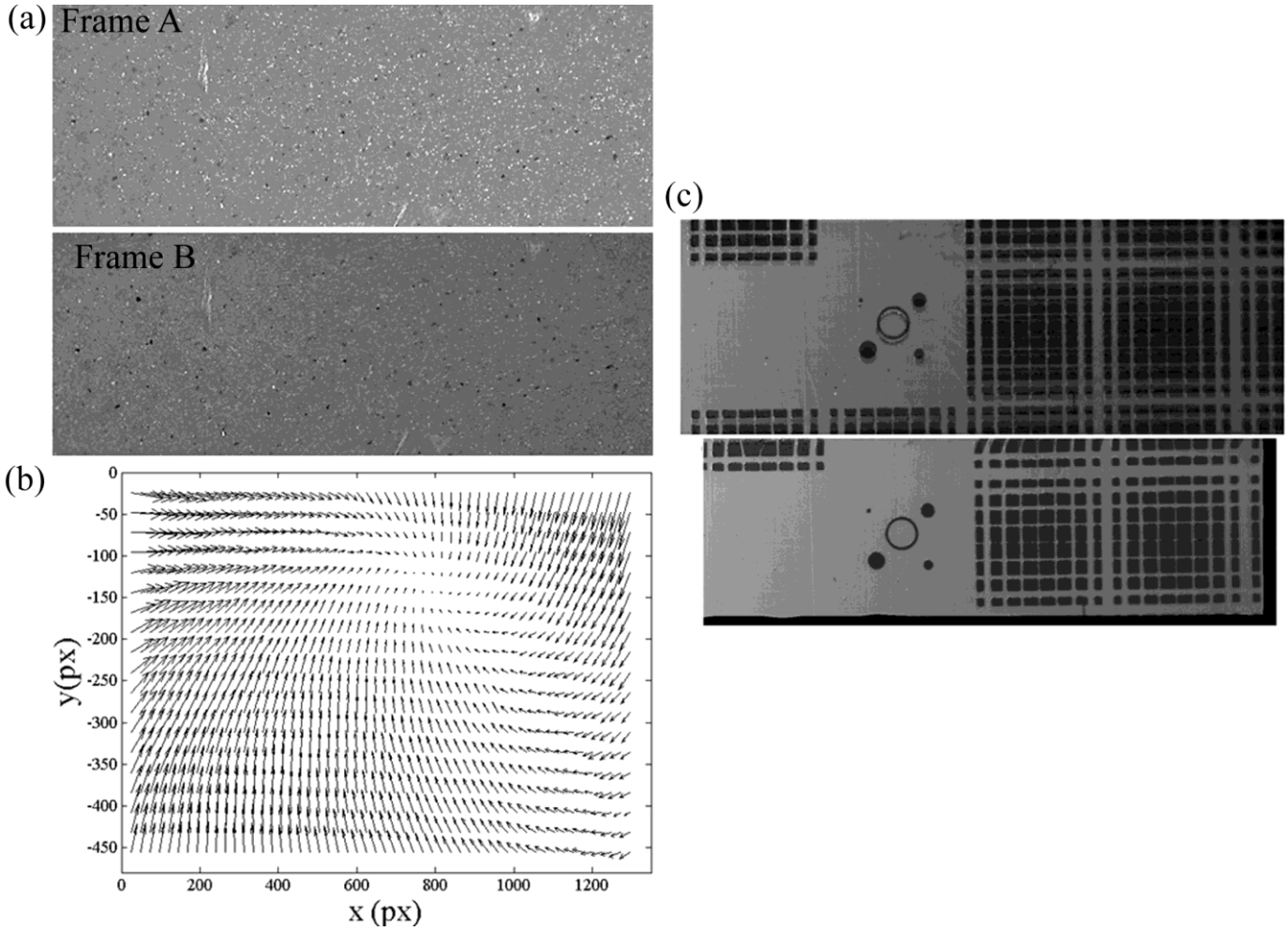

Fig. 4. (a) Sandpaper images taken as a preliminary step to resolve the sub-pixel resolution limitation of the emission splitting system. (b) PIV performed with sandpaper, where the displacement vectors are mapped from two emission images. The long wavelength image is not only shifted or rotated relative to the short wavelength image, but is also distorted. (c) Comparison of ratiometry images of a target (supplied by Photometrics) for an uncorrected secondary image (top) and a corrected secondary image with respect to the PIV displacement data (bottom).

The water temperature was varied from 25 °C to 85 °C and the corresponding Fl and the SrB intensity data were collected by taking 9-10 images for each temperature settings. Using the calibration data, the actual temperature measurements were taken in the microchannel before and after the microheater section for every power and flow rate settings, where each pixel represents an average of 9-10 recorded images.

D. Numerical Simulation for Efficiency Estimation

Numerical simulation (COMSOL Multiphysics) of the heat transfer and temperature distribution in the microchannel with integrated microheaters was performed in order to compare with the experimental results. The properties of PDMS [32], [33] were used for the microchannel device and Tin for the microheater section, and an outer sample convection coefficient of $40W/m^2 \cdot K$ was used to account for environmental loses at the outer layer of the modeled PDMS chip. This value was estimated by performing a baseline experiment at a flow rate of 15μl/min with varying convection coefficients. The value was matched with the experimental results and was applied to the rest of the simulation runs. It was determined that the convective coefficient at the external surface of the PDMS chips corresponds to forced convection conditions. This is a reasonable assumption since circulation of air was apparent near the actual setup due to the fans from the laser, power supply and the camera. Since an extra layer of PDMS slab was attached at the bottom of the PDMS chip to reduce heat loss to the environment, this was also incorporated in the model. The power supplied to the microheaters was assumed as 244mW, where an approximate lead wire resistance of 4% was accounted for from the original power input of 255mW.

III. Results

A. Corrected Ratiometric Image for Two-Color Thermometry

Prior to correlating the temperature with the image ratios, one of the two emission data must be processed so that the two microscopic images are properly aligned with each other [34]. Even though a manual mechanical alignment has been performed, its accuracy is at best to the pixel level since the procedure is performed through the use of a CCD camera. Moreover, optical distortions were observed because

of different optical paths for the short and long wavelength emissions. Due to the aforementioned reasons, the images must be pre-processed in order to match the two emission images to the sub-pixel level [25], [35], [36].

In order to align the two emission images, information on how 'distorted' one emission image is with respect to the other is required. The first frame is used as the reference frame while the second frame is the image to be corrected. A map of the displacement vector field can be acquired by imaging sandpaper (Fig. 4(a)) and performing particle image velocimetry (Insight 3G, TSI) between the two frames. As can be seen in the figure, it is apparent that there are translational, rotational, and magnifying distortions between the two images.

With the acquired PIV data, the displacement vectors between the actual pixel locations are estimated by cubic interpolation of the data throughout the entire frame (Fig. 4(b)), providing pixel by pixel resolution of the PIV distortion data. Also, the time scale is removed in the PIV data since imaging the sandpaper is performed under static conditions. Since the PIV result represents how much each pixel in the second frame has been shifted compared to the first frame, the individual pixels values (or more likely, their interpolated values) in the second frame are relocated based on the displacement information acquired from the PIV data. Once the image processing is complete, it can be assumed that in a given coordinate system, each pixel in the two frames is imaging the identical location of the actual image.

As seen in Fig. 4(c), significant difference can be observed between the ratiometry images of an uncorrected pair (top) and a corrected pair (bottom). For the uncorrected pair, shadowing effects are observed due to significant residual misalignment of the image pair. On the contrary, the ratiometry of the corrected pair results in a clear image since all the distortions and translations of the second frame have been corrected. However, it should be noted that some information is lost due to the translation of the second frame with respect to the displacement field data, as seen in the dark edges of the corrected data. It should also be noted that the corrected ratiometry image is smaller than the original image since the size of the PIV correlation map is smaller than the original image size. For the current experiment, the images were reduced by 6% in the horizontal direction and 18% in the vertical direction.

B. Identifying Source of Distortion

As mentioned in the previous section, performing PIV with sandpaper suggests that the distortion of the two emission images is unavoidable due to different optical paths. In order to identify the source of distortion, the same spatial calibration steps were repeated with different objective lens and primary dichroic mirror cubes (Table II). As can be seen in Fig. 5(a), the integrated vector plots of the sandpaper PIV results for all six cases are similar to each other. Also, Fig. 5(b), representing the variance of x-axis and y-axis components for all six cases combined passing through the dotted line in Fig. 5(a), demonstrates that the displacements of all six cases are similar. Based on the aforementioned results, it can be inferred that the image distortion mainly occurs within the emission splitting system (within the dotted line in Fig. 2(b)), where the secondary dichroic mirror, reflective mirrors and emission filters are present. If the ratiometry is performed without the spatial calibration, the uncertainty of the ratiometric image will be ~5 pixels in the x-direction and ~3 pixels in the y-direction, a significant error for experiments with limited region of interests.

TABLE II
EXPERIMENTAL PARAMETERS TO IDENTIFY SOURCE OF DISTORTION

Case	Primary dichroic mirror (Chroma)	Objective lens (Nikon Plan Fluor)
I	ZT514rdc	4X
II		10X
III		20X
IV	ZT532rdc	4X
V		10X
VI		20X

Fig. 6 represents ratiometry results of the six cases calibrated using the sandpaper PIV results from Case I only. It can be inferred from the figure that, at least for the current microscope and image splitting system combination, the ratiometry can be performed with a single PIV calibration data regardless of the changes made in the microscope, such as switching objective lens or primary dichroic mirror sets. On the contrary, the changes in the image splitting system affected the PIV correlation information. This can be seen by comparing the vector information between Fig. 4(b) and Fig. 5(a), where the vector plots are clearly different. This is due to the changes made in the image splitting system such as performing a new mechanical calibration of the system. It is thus suggested that spatial calibration be performed whenever a physical calibration is performed with the image splitting system.

To further explore that the image distortion resides at the image splitting system, the sandpaper PIV was performed without the use of the emission splitting system. For this case, two primary dichroic cube sets were mechanically switched within the microscope, a method traditionally used when performing two-color thermometry with microscopic images [19], [20]. The first dichroic mirror (ZT514rdc) cube was loaded with the short pass emission filter (λ = 522-552nm) and the second dichroic mirror (ZT532rdc) cube was loaded with the long pass emission filter (λ = 590-650nm). It should be noted that the two emission filters are the same ones used in the image splitting system for the distortion experiment. Figure 7 represents the variance of x and y vector components with respect to the total averaged x and y displacement values, respectively. The figure demonstrates that the distortion effects are much smaller than using the image splitting system since the measurement uncertainty associated with switching the dichroic cubes is 0.1 and 0.3 pixels for the x and y components, respectively. This supports the notion that the source of distortion occurs within the emission

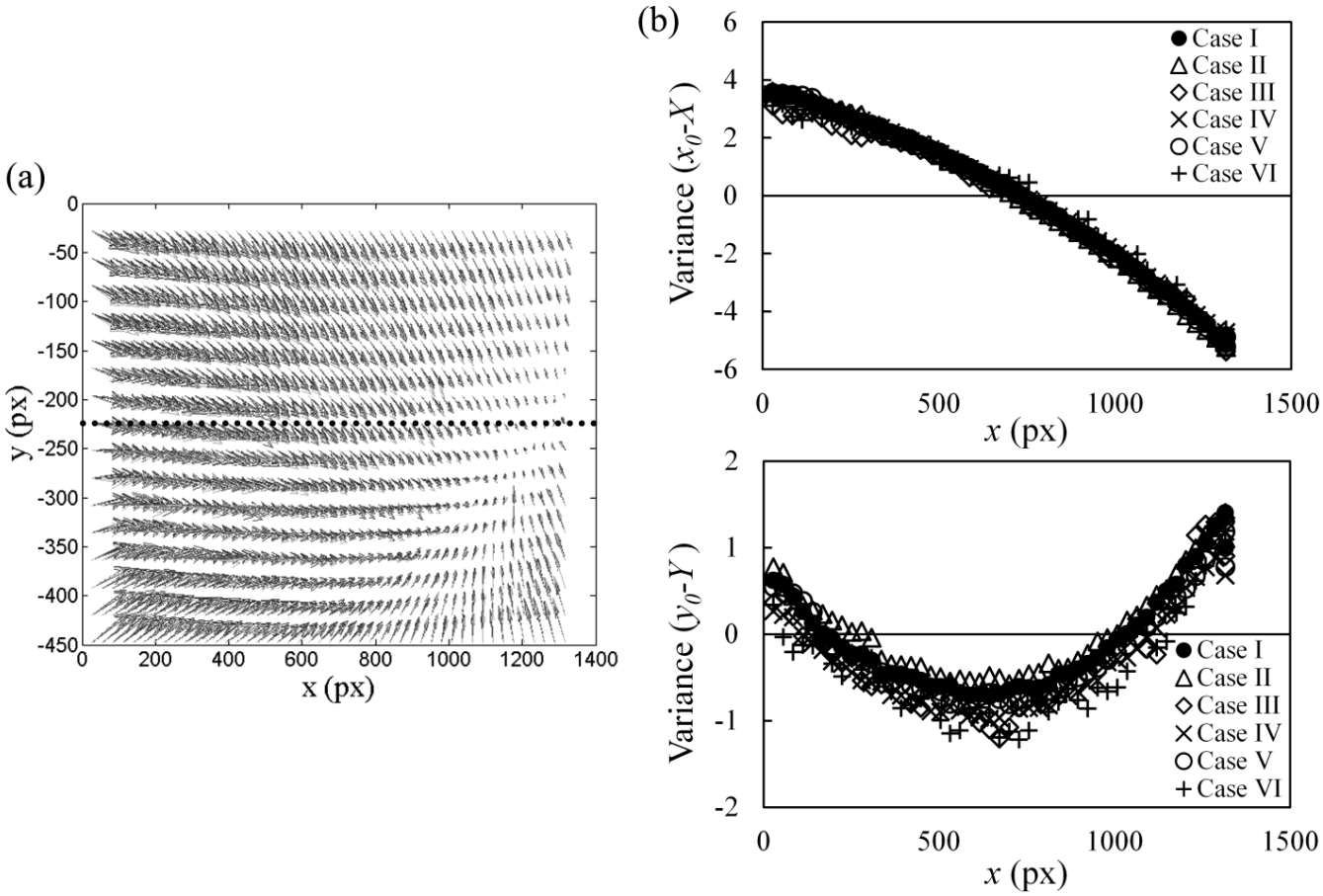

Fig. 5. (a) Integrated sandpaper PIV results of all six cases (Table I) with an interrogation spot size of 56 x 56 pixels. (b) Variance plot of x and y component vectors along the dotted line in (a). The X and Y represents the total averaged x and y displacement values.

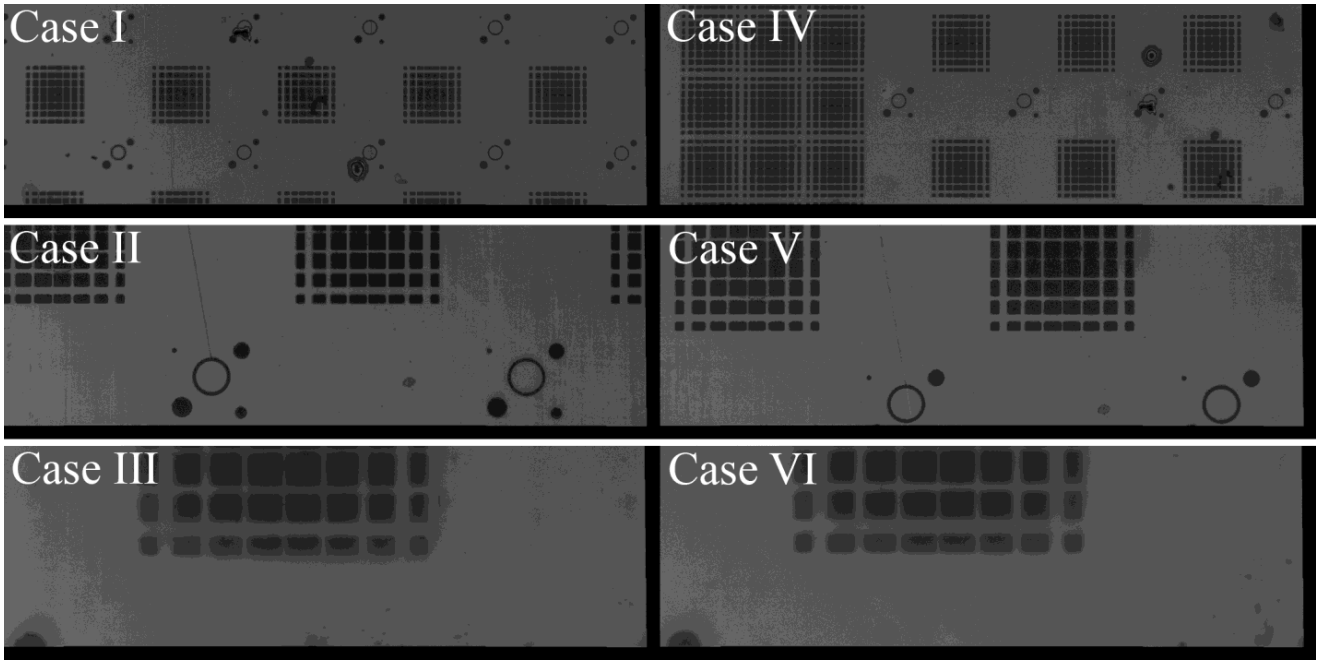

Fig. 6. Ratiometric image samples of Case I - VI with spatial calibration based on the sandpaper PIV result from Case I only. It can be seen that all the images are spatially resolved.

splitting system. Moreover, since the same set of short pass and long pass emission filters were used in both distortion experiments, it can be inferred that the distortion mainly originates from the secondary dichroic mirror and the mirror sets within the emission splitting system. While the mechanical switching method using two different dichroic cube sets

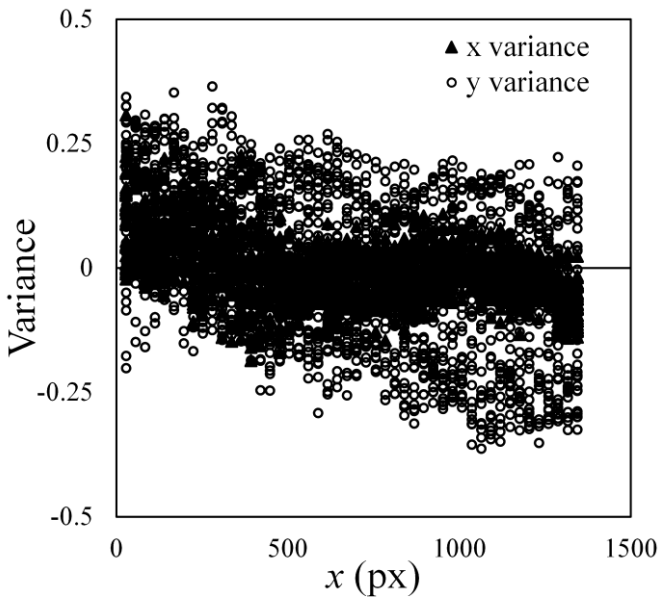

Fig. 7. Variance plot of x and y component vectors for the distortion experiment by mechanically switching the two dichroic cube sets. The graph represents vector information from the entire CCD sensor area. Compared to Fig. 5(b), the uncertainty is at least an order of magnitude smaller than using the image splitting system.

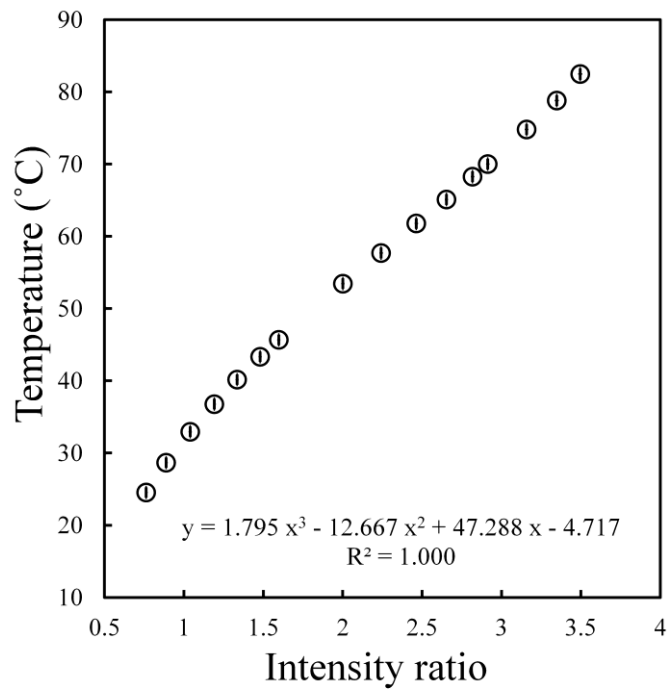

Fig. 8. Intensity ratio calibration of SrB-Fl under different temperatures. The data has been curve fitted with a parametric cubic polynomial ($R^2 = 0.9996$). The uncertainty of the temperature data is ±0.7 - 0.8 °C, which accounts for the variation in pixel intensity over the measured area.

reduces spatial distortion and seems to be a more feasible method, note must be taken that there may be significant temporal mismatch associated with this method [24], while the image splitting system delivers the two emission information simultaneously.

C. Temperature Distribution in the Microchannel

With the spatial calibration performed the intensity ratio between the Sulforhodamine-B and Fluorescein emissions are correlated as a function of temperature. This ratio was calibrated against thermocouple temperature measurements within the microchannel. A hypodermic T-type thermocouple was embedded close to the microchannel outlet and micrographs were taken for each temperature setting. The temperature T of each pixel is measured by comparing with the calibrated fluorescence intensity vs. temperature curve (Fig. 8), and the associated uncertainty of the temperature is 0.7 – 0.8 °C.

The temperature vs. intensity ratio relation is then applied to the ratiometry data (Fig. 9(a)), where the main microchannel is observable due to its high signal to noise ratio. In Fig. 9(b), the temperature profile across the microchannel is analyzed before and after the microheater section. It should be noted that the temperatures were measured 10μm away from the walls (within the gray line in Fig. 9(b)) since the temperature near the edges changed by approximately 10%. One speculation for this reason is because of photobleaching of the solution near the walls. The fluid flow is close to a no-slip boundary condition and the fluorophore solution is not likely to be adequately replenished when excited from the laser source. Also, since the true microchannel cross-section shape is trapezoidal, where the discrepancy between the top and bottom length is approximately 10%, the signal to noise ratio becomes significant near the edges of the microchannel wall. Due to the aforementioned reasons, the temperature near the edges was not accounted for in the measurement.

IV. Discussion

A. Characterization of Advective Heat Removal Efficiency

With the temperature measured using the spatially corrected images mentioned in the previous sections, the advective heat transfer efficiency η_{eff} can be experimentally determined. This efficiency is defined as,

$$\eta_{eff} = \frac{\dot{Q}_{adv}}{\dot{Q}_{electric}} \tag{3}$$

where $\dot{Q}_{adv}$ is the advective heat transfer rate and $\dot{Q}_{electric}$ is the power supplied by the joule heater. The power supplied by the heater is given by $\dot{Q}_{electric} = VI$, where V is the voltage and I is the current. The four point probe method was implemented at the junction between the microheaters and the lead wires to neglect the bias from the lead wires. For the numerator in Eq. (3), the advective heat transfer rate is $\dot{Q}_{adv} = \dot{m}\Delta(cT_m)$, where $\dot{m}$ is the mass flow rate, c is the specific heat of the water and T_m is the mixed mean bulk temperature measured before and after the microheater section (as shown in Fig. 9(a)). Since the variation in temperature across the microchannel is small and within the uncertainty ranges (Table III), the average temperature across the microchannel is suitably assumed as the bulk temperature.

Figure 10 represents advective efficiency as a function of Re, where the error bar represents the uncertainty associated with the bias and precision error, as tabulated in Table III.

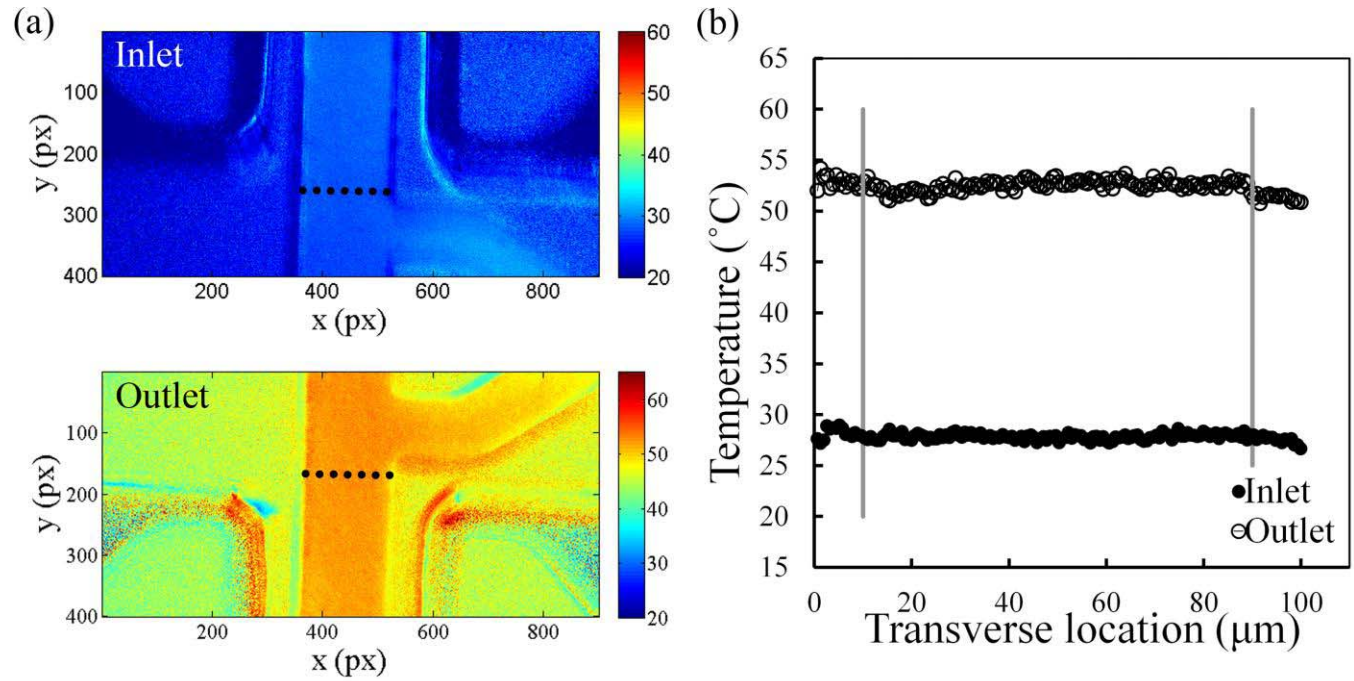

Fig. 9. (a) Plot of the calibrated temperature values applied to the ratiometry data near the inlet and the outlet. The main microchannel is distinguishable since the data is noisy outside the main microchannel, particularly where the microheaters are present. (b) An example of the temperature profile before and after the microheater section (dotted lines). The gray lines represent the actual analysis area due to possible unreliability near the microchannel.

TABLE III

COMPONENTS IN THE PROPAGATION OF UNCERTAINTY ANALYSIS FOR EFFICIENCY VS. Re ($u_T = \sqrt{B^2 + (t_{95\%} P)^2}$), WITH $t_{95\%} \sim 2$. THE PRECISION UNCERTAINTY IS BASED ON THE RANDOM ERRORS OF THE MEASUREMENT, WHERE $\delta(\Delta T) = \sqrt{(\delta T_1)^2 + (\delta T_2)^2}$ REPRESENTS THE UNCERTAINTY OF THE INLET AND OUTLET TEMPERATURE DIFFERENCE. THE BIAS UNCERTAINTY IN THE ELECTRICAL POWER TERM IS NEGLECTED SINCE THE CONTRIBUTION TO THE TOTAL UNCERTAINTY IS $<<1\%$

η					Re					
Bias (B)		Precision (P)			Bias (B)			Precision (P)		
$\frac{\delta Q}{Q}$	$\frac{\delta(\Delta T)}{\Delta T}$	$\frac{\delta Q}{Q}$	$\frac{\delta(\Delta T)}{\Delta T}$	$\frac{\delta(VI)}{VI}$	$\frac{\delta Q}{Q}$	$\frac{\delta A}{A}$	$\frac{\delta D_h}{D_h}$	$\frac{\delta Q}{Q}$	$\frac{\delta A}{A}$	$\frac{\delta D_h}{D_h}$
0.05	0.04 – 0.11	0.01– 0.02	0.02 – 0.09	0.06	0.05	0.03	0.04	0.01 – 0.02	0.06	0.06

The figure shows good agreement between the experimental and numerical results and indicates that the efficiency increases with increasing flow rate. As can be seen in the figure, there are limitations on how much the advective efficiency can increase with advective transport. The advective efficiency increases with increasing flow rate due to the decreasing advective resistance $R_{adv} = 1/\dot{m}c_p$, but starts to level off as $Re > 20$. In order to explore this behavior, a thermal circuit analogy is implemented to compare the experimental results with the numerical results. The effective resistances as a function along the microchannel are,

$$R_{conv} = \frac{1}{\int_0^A h dA} = \left(\int_0^A \frac{q''_{conv}}{T_s - T_b} dA\right)^{-1} \tag{4a}$$

$$R_{cond} = \frac{1}{\int_0^A \frac{k_{PDMS}}{t} dA} = \left(\int_0^A \frac{q''_{conv}}{T_h - T_s} dA\right)^{-1} \tag{4b}$$

$$R_{loss} = \left(\int_0^A \frac{q''_{heater} - q''_{conv}}{T_h - T_\infty} dA\right)^{-1} \tag{4c}$$

for convective resistance, conductive resistance through the walls, and heat loss resistance to the environment, respectively. As can be seen in the thermal circuit diagram (Fig. 11(a)), the heat is generated in the microheater section and is split into two directions. In one direction, the generated electrical heat is transported through the microchannel by conduction through the PDMS walls and then convection/advection, while the rest is rejected to the environment as heat loss. For the heat transported through the microchannel, the three thermal resistances R_{cond}, R_{conv} and R_{adv} are coupled with each other in series. Results suggest that the heat lost to the environment is significant despite the fact that PDMS is known to have poor conductivity ($\sim 0.25 W/m \cdot K$). Particularly for $Re < 20$, the advective resistance is significantly higher than the other heat

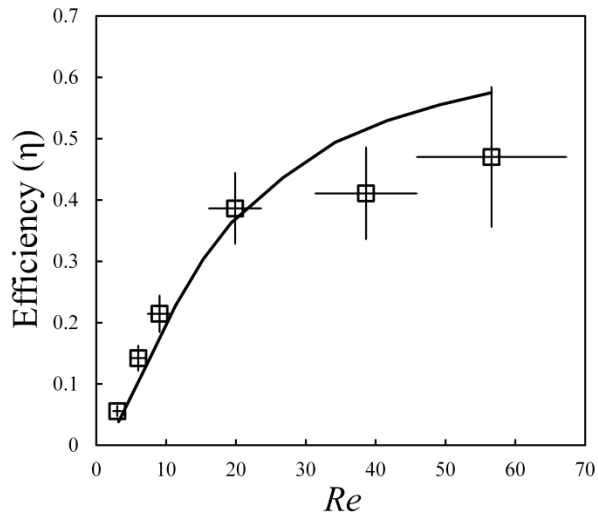

Fig. 10. Efficiency vs. flow rate for ∼250mW electrical heat input to the microheaters, where the square boxes are the experimental results and the solid line is the numerical results. The uncertainty is larger for higher flow rates and smaller power input. This is due to the uncertainty associated with the thermal measurement (0.5–1.0 °C), where a smaller temperature difference will significantly increase the error of the efficiency. It should be noted that the entrance effects are negligible since the maximum hydrodynamic and thermal entrance lengths are calculated to be approximately 1% and 5%, respectively.

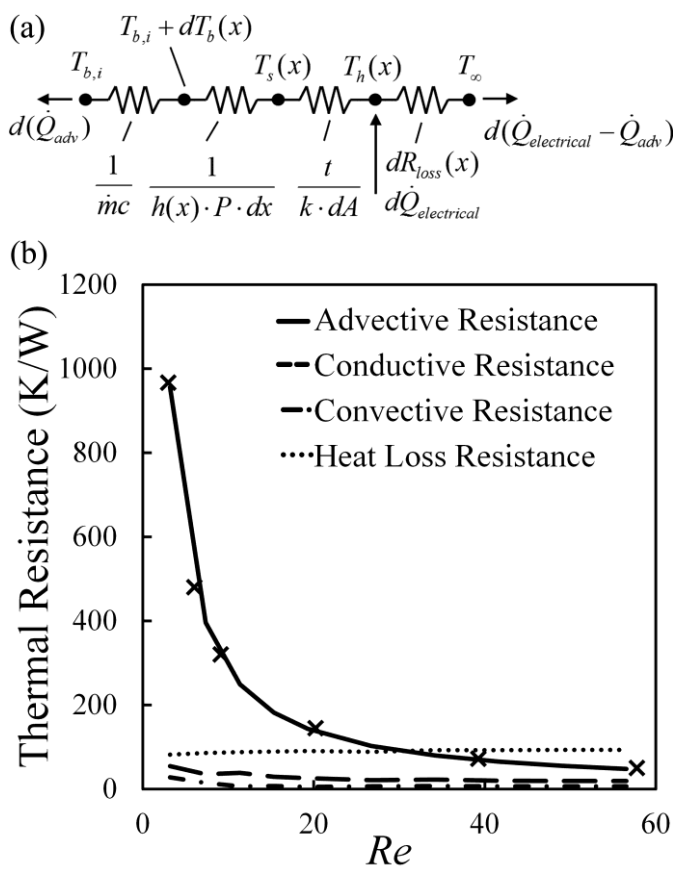

Fig. 11. (a) Thermal circuit diagram of the system and (b) graph of numerical results on thermal resistance vs. flow rate for different heat transfer modes. Majority of the resistance resides on the advective resistance for $Re < 20$. The experimental data for the advective resistance are included for comparison.

loss components (Fig. 11(b)), thus resulting in an advective efficiency under 30% where the majority of the Joule heating will escape to the environment.

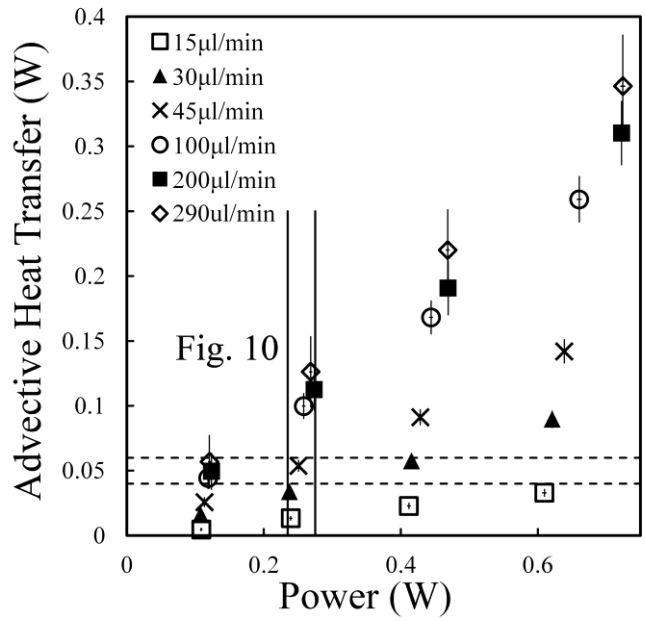

Fig. 12. Plot on advective heat transfer vs. electrical power supplied to the microheaters. The solid line is where the power supplied through the heater is maintained at ∼244mW (Fig. 10), while the dashed line represents the input power required to maintain constant heat flux through the microchannel walls.

Since the advective efficiency is highly dependent on *Re* under relatively low *Re* conditions, caution must be taken when assuming constant power input to the microchannel for different flow rates while using Joule heating. An example can be seen from the data within the solid lines in Fig. 12, which represents the measured advective heat transfer as a function of electrical power input under varying flow rate conditions. Within the solid lines, the electrical power input is maintained at ∼255mW. However, the heat conducted through the microchannel walls (identical to the advective heat transfer) is not maintained due to the changing advective thermal resistance. Since the heat path is determined by the thermal resistances, the drastically changing advective resistance makes it difficult to maintain a consistent power input to the microchannel.

To ensure a constant power input to the microchannel under varied flow rates, the electrical power input to the microheaters must vary accordingly as well. For example, in order to maintain an average of 50mW of power to the microchannel, the power supplied through the microheaters should vary between 100mW - 700mW (data within the dashed lines in Fig. 12). As the power supplied to the microheaters varies by nearly an order of magnitude, care must be taken when assuming constant power input conditions, particularly for microfluidic applications where the advective transport is small.

As a side note, while the combined conductive and convective heat transfer resistance is less significant for $Re < 20$, they become comparable to the advective resistance for $Re > 20$ as the advective resistance diminishes by $dR_{adv}/d\dot{m} = -1/\dot{m}^2$. As the mass flow rate is increased, the advective resistance reduces by ∼10% between $20 < Re < 60$ and is likely to top off at ∼80% with increasing flow rate (Fig. 11(b)) as the

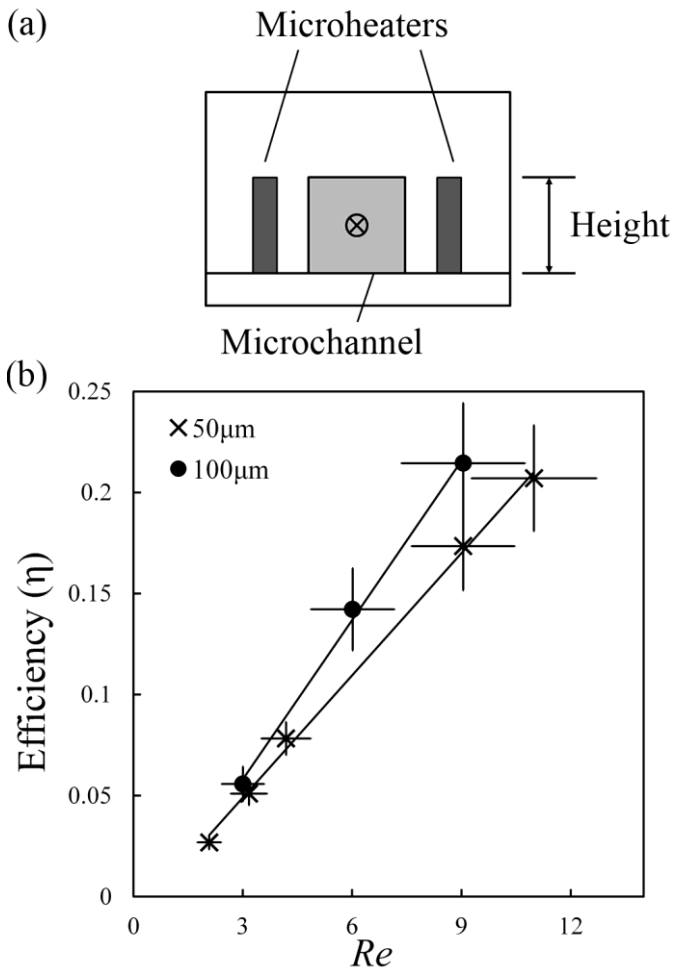

Fig. 13. (a) Schematic diagram and (b) graph of heating efficiency vs. flow rate comparison for two different microchannel/microheater heights, 50μm and 100μm. The linear curve fitted line is shown to enhance visualization of the trends.

combined convective, conductive and advective resistance balances with the heat loss resistance. However, since increasing the flow rate Q in microchannels becomes difficult due to a large pressure drop requirements ($\Delta P/Q \sim 1/D_h^4$), and since the Re $\sim$60 in this experiment corresponds to 300μl/min, it is likely that the advective resistance will be the dominant parameter to characterize the heat removal efficiency for most microfluidic applications.

B. Microheater Dimension Effects on Advective Efficiency

One method to increase the advective efficiency is to increase the area of the microchannel wall that receives heat from the microheaters. In Fig. 13, microheaters with height to width aspect ratio of 1.3 and 2.5 (microchannel heights of 50μm and 100μm, respectively) are compared under an input power of $\sim$250mW. Since a constant pressure source was used to drive the fluid flow, the flow rate was limited in the smaller aspect ratio microchannel, where $Re < 12$. The data was linearly fitted to provide a general overview on the efficiency comparison between the two aspect ratio microchannels.

Comparison between the ratio of the two linear regressions suggest that the efficiency vs. flow rate is increased by 30% with an increase in microheater aspect ratio from 1.3 to 2.5, which is expected since more microheater surface area is exposed to the main microchannel.

V. Conclusion

The results presented here highlight the importance of spatial calibration in performing two-color fluorescence thermometry for microfluidic applications. Using particle image velocimetry (PIV) on a sandpaper image to obtain the local distortion information, the second image was reconstituted with respect to the first image, or the reference image. From the PIV results, it was apparent that there were translational, rotational, and magnifying distortions between the two images. Moreover, results showed that the source of distortion is in the emission splitting system itself, where the secondary dichroic mirror and reflective mirrors reside. If the spatial calibration is not performed, the uncertainty of the pixel location will be $\sim$5 pixels and $\sim$3 pixels in the x and y components, respectively. Since the region of interest when imaging microchannels is usually limited, the uncertainty is significant and it is necessary to perform spatial calibration when using an emission splitting system.

With the spatial calibration applied to each ratiometric images, experimental results showed good agreement with numerical results, where the temperature under varying flow rates in a microchannel with heated side walls was characterized. Results show that the advective efficiency is a function of Re and that the electrical power supplied to the microheaters may need to be varied by $\sim O(10)$ in order to maintain constant power through the microchannel walls. Based on the PIV results and comparison with the heat transfer experiments, spatial calibration is shown to be significantly important when using the emission splitting system for two-color thermometry.

References

[1] D. Erickson and D. Li, "Integrated microfluidic devices," *Anal. Chim. Acta*, vol. 507, no. 1, pp. 11–26, 2004.
[2] Y. Peles, A. Koşar, C. Mishra, C. J. Kuo, and B. Schneider, "Forced convective heat transfer across a pin fin micro heat sink," *Int. J. Heat Mass Transf.*, vol. 48, no. 17, pp. 3615–3627, 2005.
[3] C. Harris, K. Kelly, T. Wang, A. McCandless, and S. Motakef, "Fabrication, modeling, and testing of micro-cross-flow heat exchangers," *J. Microelectromech. Syst.*, vol. 11, pp. 726–735, Dec. 2002.
[4] M. Lee, M. Wong, and Y. Zohar, "Integrated micro-heat-pipe fabrication technology," *J. Microelectromech. Syst.*, vol. 12, no. 2, pp. 138–146, 2003.
[5] B. Carroll and C. H. Hidrovo, "Droplet collision mixing diagnostics using single fluorophore LIF," *Experim. Fluids*, vol. 53, no. 5, pp. 1301–1316, 2012.
[6] S. H. Wong, M. C. L. Ward, and C. W. Wharton, "Micro T-mixer as a rapid mixing micromixer," *Sens. Actuators B, Chem.*, vol. 100, pp. 359–379, Jan. 2004.
[7] J. Khandurina, T. E. McKnight, S. C. Jacobson, L. C. Waters, R. S. Foote, and J. M. Ramsey, "Integrated system for rapid PCR-based DNA analysis in microfluidic devices," *Anal. Chem.*, vol. 72, no. 13, pp. 2995–3000, 2000.
[8] E. T. Lagally, P. C. Simpson, and R. A. Mathies, "Monolithic integrated microfluidic DNA amplification and capillary electrophoresis analysis system," *Sens. Actuators B, Chem.*, vol. 63, no. 3, pp. 138–146, 2000.
[9] B. D. DeBusschere and G. T. A. Kovacs, "Portable cell-based biosensor system using integrated CMOS cell-cartridges," *Biosensors Bioelectron.*, vol. 16, nos. 7–8, pp. 543–556, 2001.

[10] P. J. Hung, P. J. Lee, P. Sabounchi, N. Aghdam, R. Lin, and L. P. Lee, "A novel high aspect ratio microfluidic design to provide a stable and uniform microenvironment for cell growth in a high throughput mammalian cell culture array," *Lab Chip*, vol. 5, pp. 44–48, Jan. 2005.
[11] T.-J. Kim, S.-J. Kim, and H. I. Jung, "Physical stimulation of mammalian cells using micro-bead impact within a microfluidic environment to enhance growth rate," *Microfluidics Nanofluidics*, vol. 6, no. 1, pp. 131–138, 2009.
[12] H. Wu and P. Cheng, "An experimental study of convective heat transfer in silicon microchannels with different surface conditions," *Int. J. Heat Mass Transf.*, vol. 46, no. 14, pp. 2547–2556, 2003.
[13] W. Qu, G. M. Mala, and D. Li, "Heat transfer for water flow in trapezoidal silicon microchannels," *Int. J. Heat Mass Transf.*, vol. 43, no. 21, pp. 3925–3936, 2000.
[14] P. S. Lee, S. V. Garimella, and D. Liu, "Investigation of heat transfer in rectangular microchannels," *Int. J. Heat Mass Transf.*, vol. 48, no. 9, pp. 1688–1704, 2005.
[15] L. Zhang *et al.*, "Measurements and modeling of two-phase flow in microchannels with nearly constant heat flux boundary conditions," *J. Microelectromech. Syst.*, vol. 11, pp. 12–19, Feb. 2002.
[16] J. Coppeta and C. Rogers, "Dual emission laser induced fluorescence for direct planar scalar behavior measurements," *Experim. Fluids*, vol. 25, no. 1, pp. 1–15, 1998.
[17] J. Sakakibara, K. Hishida, and M. Maeda, "Measurements of thermally stratified pipe flow using image-processing techniques," *Experim. Fluids*, vol. 16, no. 2, pp. 82–96, 1993.
[18] D. Ross, M. Gaitan, and L. E. Locascio, "Temperature measurement in microfluidic systems using a temperature-dependent fluorescent dye," *Anal. Chem.*, vol. 73, no. 17, pp. 4117–4123, 2001.
[19] M. Kim and M. Yoda, "Dual-tracer fluorescence thermometry measurements in a heated channel," *Experim. Fluids*, vol. 49, no. 1, pp. 257–266, 2010.
[20] V. Natrajan and K. Christensen, "Non-intrusive measurements of convective heat transfer in smooth-and rough-wall microchannels: Laminar flow," *Experim. Fluids*, vol. 49, no. 5, pp. 1021–1037, 2010.
[21] J. Sakakibara and R. Adrian, "Whole field measurement of temperature in water using two-color laser induced fluorescence," *Experim. Fluids*, vol. 26, nos. 1–2, pp. 7–15, 1999.
[22] S. M. Soloff, R. J. Adrian, and Z.-C. Liu, "Distortion compensation for generalized stereoscopic particle image velocimetry," *Meas. Sci. Technol.*, vol. 8, no. 12, p. 1441, 1997.
[23] C. H. Hidrovo and D. P. Hart, "Emission reabsorption laser induced fluorescence (ERLIF) film thickness measurement," *Meas. Sci. Technol.*, vol. 12, no. 4, p. 467, 2001.
[24] V. Natrajan and K. Christensen, "Two-color laser-induced fluorescent thermometry for microfluidic systems," *Meas. Sci. Technol.*, vol. 20, no. 1, p. 015401, 2008.
[25] A. C. Siegel, D. A. Bruzewicz, D. B. Weibel, and G. M. Whitesides, "Microsolidics: Fabrication of three-dimensional metallic microstructures in poly (dimethylsiloxane)," *Adv. Mater.*, vol. 19, no. 5, pp. 727–733, 2007.
[26] R. L. Webb, E. R. G. Eckert, and R. J. Goldstein, "Heat transfer and friction in tubes with repeated-rib roughness," *Int. J. Heat Mass Transf.*, vol. 14, no. 4, pp. 601–617, 1971.
[27] T. J. Kim and C. H. Hidrovo, "Pressure and partial wetting effects on superhydrophobic friction reduction in microchannel flow," *Phys. Fluids*, vol. 24, no. 11, pp. 112003-1–12003-18, 2012.
[28] T. J. Kim, R. Kanapuram, A. Chhabra, and C. H. Hidrovo, "Thermo-wetting and friction reduction characterization of microtextured superhydrophobic surfaces," *J. Fluids Eng.*, vol. 134, no. 11, p. 114501, 2012.
[29] W. W. Y. Chow, K. F. Lei, G. Shi, W. J. Li, and Q. Huang, "Microfluidic channel fabrication by PDMS-interface bonding," *Smart Mater. Struct.*, vol. 15, no. 1, p. S112, 2005.
[30] M. E. Steinke and S. G. Kandlikar, "Control and effect of dissolved air in water during flow boiling in microchannels," *Int. J. Heat Mass Transf.*, vol. 47, no. 8, pp. 1925–1935, 2004.
[31] J. Lou, T. A. Hatton, and P. E. Laibinis, "Fluorescent probes for monitoring temperature in organic solvents," *Anal. Chem.*, vol. 69, no. 6, pp. 1262–1264, 1997.
[32] B. Yang and Q. Lin, "A latchable microvalve using phase change of paraffin wax," *Sens. Actuators A, Phys.*, vol. 134, no. 1, pp. 194–200, 2007.
[33] Z. Han and A. Fina, "Thermal conductivity of carbon nanotubes and their polymer nanocomposites: A review," *Progr. Polymer Sci.*, vol. 36, no. 7, pp. 914–944, 2011.
[34] C. H. Hidrovo, "2D thickness and temperature mapping of fluids by means of a two-dye laser induced fluorescence ratiometric scheme," *J. Flow Vis. Image Process.*, vol. 9, nos. 2–3, pp. 1–21, 2002.
[35] M. David, D. Fogg, C. H. Hidrovo, R. Flynn, and K. Goodson, "Development and calibration of a two-dye fluorescence system for use in two-phase micro flow thermometry," in *Proc. 10th Intersoc. Conf. Thermal Thermomech. Phenomena Electron. Syst.*, 2006, pp. 79–86.
[36] C. H. Hidrovo, R. R. Brau, and D. P. Hart, "Excitation nonlinearities in emission reabsorption laser-induced fluorescence techniques," *Appl. Opt.*, vol. 43, no. 4, pp. 894–913, 2004.

Tae Jin Kim (M'14) received the Ph.D. from the University of Texas at Austin in 2013. He is a postdoctoral research associate in the Mechanical and Industrial Engineering Department at Northeastern University. His current research interests include thermal-fluids systems, multiphase flow, optical diagnostics, microfabrication and biological applications.

Myeongsub Kim received the Ph.D. from the Georgia Institute of Technology in 2011. He is a postdoctoral fellow in the Mechanical Engineering Department at the University of Texas at Austin. He was a postdoctoral fellow at the University of Toronto, Canada, from 2011 to 2012. His current research interests include optofluidics, thermal-energy systems, thermal management, diagnostic techniques related to thermal-fluid sciences, oil and gas, and biological and energy applications.

Sungyun Hann is expected to receive the B.S. degree in May 2014 from the University of Texas at Austin in Mechanical Engineering. His current research interest aligns with micro-scale fluid characterization with material fabrication processes, as well as advanced space propulsion systems. He will pursue his graduate-level research at University of California, Los Angeles, in September 2014.

Juan Trejo, photograph and biography not available at the time of publication.

Carlos H. Hidrovo recieved the Ph.D. in Mechanical Engineering from the Massachusetts Institute of Technology in 2001. He is an assistant professor in the Mechanical and Industrial Engineering Department at Northeastern University. He worked as a research scientist in the 3D Optical Systems group at MIT, as a research associate in the Micro Heat Transfer Laboratory at Stanford University, and as an assistant professor in the Mechanical Engineering Department at UT Austin before joining the faculty of Northeastern University in January of 2014. He is the recipient of a 2012 NSF CAREER Award from the Fluid Dynamics program, the 2008 DARPA Young Faculty Award, and the American Society of Mechanical Engineering 2001 Robert T. Knapp Award. Dr. Hidrovo's current research interests lie at the intersection of multiscale and multiphase flow and transport phenomena, surface tension interactions in micro/nanoengineered structures, and electrokinetic ion transport in porous media for applications in energy storage, portable biochemical diagnostics, thermal management, and water treatment systems.